condensed matter

MDPI

Article

Enhancing the Photoelectrochemical Performance of a Superlattice p–n Heterojunction $CuFe_2O_4/ZnFe_2O_4$ Electrode for Hydrogen Production

M. K. Al Turkestani

Department of Physics, Umm Al-Qura University, Makkah 24382, Saudi Arabia; mkturkestani@uqu.edu.sa

Abstract: A p–n heterojunction film consisting of p-type $CuFe_2O_4$ and n-type $ZnFe_2O_4$ was fabricated in this study. The n-type $ZnFe_2O_4$ film was deposited on a stainless steel substrate using the spray pyrolysis method, after which a top layer of p-type $CuFe_2O_4$ thin film was deposited and annealed. Characterization techniques, such as X-ray diffraction, scanning electron microscopy, UV–Vis diffuse reflectance spectroscopy, and photoluminescence, confirmed the formation of a superlattice p–n heterojunction between $CuFe_2O_4$ and $ZnFe_2O_4$. Photoelectrochemical measurements were conducted to investigate the photoelectrochemical properties of the samples, resulting in a photocurrent of 1.2 mA/cm^2 at 1.5 V (vs. Ag/AgCl) under illumination from a 100-watt LED light source. Utilizing the p–n junction of $CuFe_2O_4/ZnFe_2O_4$ as a photoanode increased the hydrogen production rate by 30% compared to that of the dark measurement. This enhancement in performance was attributed to the potential barrier at the p–n heterojunction interface, which improved the separation of photoinduced electron–hole pairs and facilitated a more efficient charge transfer. Additionally, coating the stainless steel electrode with this ferrite sample improved both the corrosion resistance and the stability of hydrogen production over extended operation times.

Keywords: p–n junction; hydrogen evolution; corrosion; photoelectrochemical cell; electrolysis

Citation: Al Turkestani, M.K. Enhancing the Photoelectrochemical Performance of a Superlattice p–n Heterojunction $CuFe_2O_4/ZnFe_2O_4$ Electrode for Hydrogen Production. *Condens. Matter* **2024**, *9*, 31. https://doi.org/10.3390/condmat9030031

Academic Editor: Bohayra Mortazavi

Received: 3 July 2024
Revised: 24 July 2024
Accepted: 25 July 2024
Published: 26 July 2024

1. Introduction

Producing hydrogen as an alternative source of clean energy has become a significant challenge [1,2]. Photoelectrochemical cells (PECs) have been extensively studied since it was discovered that TiO_2 can split water under UV irradiation [3–6]. However, these PEC cells have limited efficiency due to the use of UV radiation, which accounts for only 4% of the total solar irradiation spectrum. To improve hydrogen production under solar light, which contains a large portion (43%) of visible radiation [7,8], there is a need to develop a new photocatalyst with a smaller energy gap in the visible range, chemical stability, low electron–hole recombination rate, and nontoxic properties.

Magnetic spinel ferrites (MFe_2O_4; M = Cu, Ni, Cd, Ca, Zn, etc.) have emerged as promising materials for hydrogen production [9,10]. These ferrites exhibit high thermal and chemical stability [11–13] and possess a narrow energy gap in the visible range [14–16], making them suitable for photocatalysis and applications involving solar water splitting [17–20]. Combining p-type ferrites with n-type semiconductors to form p–n heterojunctions, such as $CuFe_2O_4/CdS$, $CuFe_2O_4/SnO_2$, $CuFe_2O_4/TiO_2$, $CaFe_2O_4/WO_3$, $CaFe_2O_4/BiVO_4$, and $CsFe_2O_4/Fe_2O_3$, has improved PEC performance compared to bare n-type materials [21–27]. The enhanced photocatalytic activity is attributed to the separation of photogenerated electron–hole pairs by the internal potential barrier at the p–n heterojunction interface. However, the challenge lies in the chemical and physical structure mismatch between the p-type and n-type materials, resulting in low PEC cell efficiency due to defects in the interface.

In this paper, a superlattice heterojunction between p-type $CuFe_2O_4$ and n-type $ZnFe_2O_4$ is investigated as a photoanode for hydrogen production. Using these ferrites

offers several advantages: (1) they have the same chemical and crystal structure, (2) their lattice mismatch is minimal, (3) their energy gaps are in the visible range, and (4) they are expected to generate a high internal potential at the p–n junction interface.

Throughout this study, we employed various techniques to characterize the structural and optical properties of the samples. Additionally, linear sweep voltammetry (LSV) was used to evaluate the performance of the PEC cell, and the hydrogen production rate was monitored over an extended period of operation time.

2. Sample Preparation

2.1. Preparation of $CuFe_2O_4$ and $ZnFe_2O_4$ Films on Stainless Steel Sheets

$CuFe_2O_4$ and $ZnFe_2O_4$ films were fabricated on stainless steel 304 plates using the spray pyrolysis technique. Initially, the stainless steel sheets were cut into 5 cm × 5 cm pieces. To increase the surface area, the plates were etched with 1200 grinding papers for 5 min. Then, the plates underwent ultrasonic cleaning in ethanol and deionized water for 10 min each. Finally, the stainless steel plates were dried using a hot air path to prepare them for the next steps. For depositing the desired metal ferrites, $Fe(NO_3)_3{\cdot}7H_2O$, Cu(NO3)2·$5H_2O$, and $Zn(NO_3)_2{\cdot}6H_2O$ salts from Merck India with 98% purity were utilized as sources of Fe, Cu, and Zn ions, respectively. All chemicals were from the molar ratios of Fe:Zn and Fe:Cu, which were maintained at 2:1. The solvent used in this study was a mixture of water and ethanol with a volume ratio of 3:1. The solution was sprayed on stainless steel plates using an ultrasonic nebulizer at a temperature of 350 °C. Finally, the deposited ferrite films were annealed using air heated to 500 °C for 2 h. The thickness of the prepared films was controlled by the deposition time. The film thickness was estimated using the weight difference method, revealing that a deposition time of 30 min resulted in films with a thickness of 2 μm.

2.2. Preparation of $CuFe_2O_4$/$ZnFe_2O_4$ P–N Junction

One of the annealed Zn ferrite films with a thickness of 2 μm served as the substrate for depositing the Cu ferrite film using the same steps, except that the deposition time was reduced to 15 min, and the annealing temperature was set to 450 °C for 1 h. The thickness of the Cu ferrite film was approximately 200 nm. Confirmation of the $CuFe_2O_4/ZnFe_2O_4$ p–n junction formation was achieved by measuring the electric resistance in forward bias (indicating low resistance) and reverse bias (indicating high resistance).

2.3. Characterization Techniques

In this study, the crystal structure and phase identification were investigated using the X-ray diffractometer Philips model (PW-1710, Philips, Amsterdam, The Netherlands) with Cu-Kα radiation (λ = 1.5406 Å). The surface morphologies of the thin films were examined using field emission scanning electron microscopy. To determine the bandgap energy value, the thin films were examined using a UV–Vis model JASCO 670 spectrophotometer (Jasco, Tokyo, Japan) within the wavelength range of 200–800 nm. The electrochemical performances of the deposited films were assessed in a standard three-electrode cell at room temperature. The anode electrode was prepared for each of the thin films, a graphene electrode served as the counter electrode, and an Ag/AgCl reference electrode was employed.

Electrochemical impedance spectroscopy (EIS) and Mott–Schottky plots were carried out using a TEGAM LRC Meter Model 3550 (TEGAM, Geneva, OH, USA). Cyclic voltammetry (CV) studies of the samples were conducted in a 0.3 M NaOH aqueous electrolyte using a specially designed linear sweep voltammetry (LSV) device. This LSV device was calibrated using an electrochemical workstation (Potentiostat/Galvanostat PARSTAT 2273 model, Princeton Applied Research, Oak Ridge, TN, USA). The hydrogen production rate was measured by connecting the generator to an inverted measuring cylinder for a specific period to quantify the production rate.

3. Results and Discussion

3.1. X-ray Diffraction Measurements

Figure 1 presents the X-ray diffraction (XRD) patterns obtained for the prepared samples. The XRD patterns of the bare stainless steel exhibit characteristic peaks corresponding to the stainless steel's 304 phase. Specifically, the peaks observed at 34°, 51°, and 74° can be attributed to the face-centered cubic (FCC) structure of stainless steel 304 [28]. For the ferrite samples, the XRD patterns indicate the formation of a single-spinel cubic-phase structure on the stainless steel substrate. By applying Bragg's law and the Williamson–Hall equation to the three most intense peaks, various parameters, such as the lattice parameter, crystallite size, and microstrain, were calculated and are listed in Table 1.

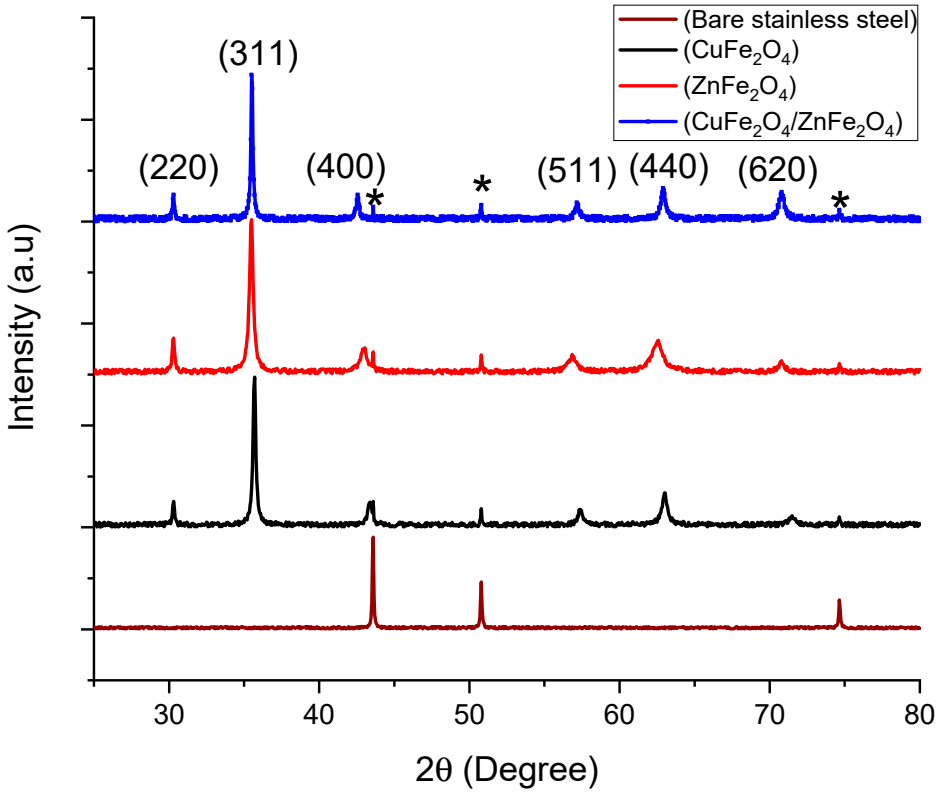

Figure 1. XRD patterns for the prepared samples. * indicates the peaks for stainless steel substrate.

Table 1. Lattice parameter, crystallite size, and microstrain of the prepared samples.

Sample	Lattice Parameter (Å)	Crystallite Size (nm)	Microstrain
$ZnFe_2O_4$	8.425	23	0.005
$CuFe_2O_4$	8.384	39	0.002
$CuFe_2O_4/ZnFe_2O_4$	8.416	47	0.011

It is evident that the lattice parameter of Zn ferrite (a_{Zn} = 8.425 Å) is greater than that of Cu ferrite (a_{Cu} = 8.384 Å) [29,30]. This difference can be attributed to the larger ionic radius of Zn^{2+} (0.78 nm) compared to that of Cu^{2+} (0.65 nm). Furthermore, the crystallite size of Cu ferrite is larger than that of Zn ferrite, indicating a higher degree of crystallinity in Cu ferrite.

Additionally, the lattice parameter of the $CuFe_2O_4/ZnFe_2O_4$ sample was between a_{Zn} and a_{Cu} but leaned toward a_{Zn}. However, the microstrain showed a significant increase. These results confirm the presence of a superlattice structure consisting of Cu ferrite film on Zn ferrite. The increased microstrain can be attributed to the lattice mismatch ($\Delta a/a_{Zn}$ =

($a_{Zn} - a_{Cu})/a_{Zn}$ = 1%) between Cu ferrite and Zn ferrite. Finally, the crystallite size of this sample is greater than that of both Cu ferrite and Zn ferrite, indicating an enhancement in the crystallinity of the Cu ferrite film when grown on Zn ferrite, with the Zn ferrite crystals acting as seeds for the growth of the Cu ferrite film.

3.2. Optical Absorption and Photoluminescence

The diffuse reflection method was employed to determine the optical bandgap of the prepared samples. Figure 2 illustrates the reflection coefficient (R) of all the investigated samples in the UV–Vis range.

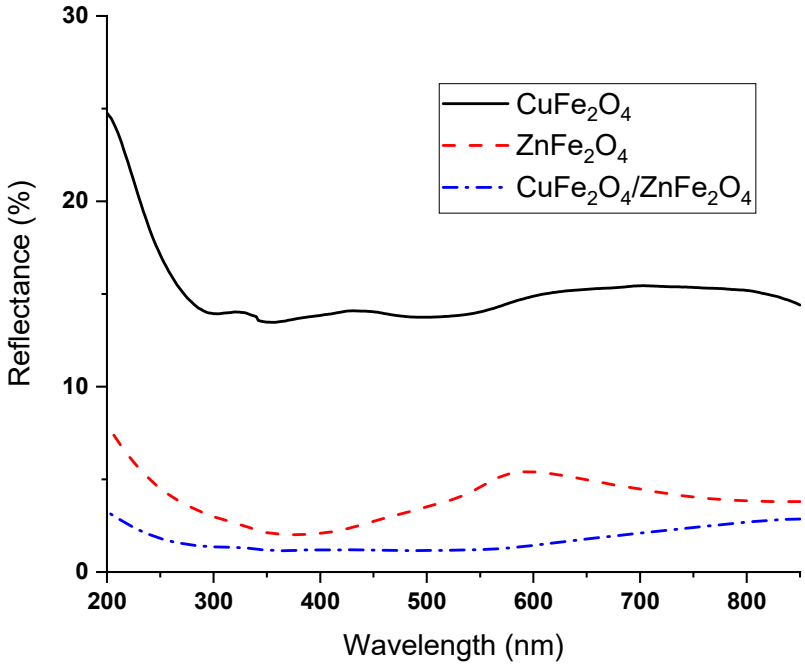

Figure 2. Diffuse reflection spectra for the prepared samples.

The absorption coefficient (α) can be estimated using the following Kubelka–Munk equation [31]:

$$\alpha = (1 - R)^2/2R$$

The direct energy gap of the prepared sample can be determined using Tauc's relation [32], expressed as follows:

$$(\alpha h\nu)^2 = A(h\nu - E_g)$$

Here, A represents a constant, $h\nu$ denotes the photon energy, and E_g represents the optical direct energy gap.

Figure 3 displays Tauc's relation between $(\alpha h\nu)^2$ and $h\nu$. The energy gap can be determined by identifying the intersections of the lines with $h\nu$ axis. It was observed that the energy gap of Zn ferrite was 2.49 eV, while that of Cu ferrite was 2.04 eV (inset figure). These results are consistent with previous reports [33–35]. For the $CuFe_2O_4/ZnFe_2O_4$ sample, it is crucial to note the presence of two transition states corresponding to Cu ferrite and Zn ferrite. It is well established that $CuFe_2O_4$ is a p-type semiconductor with a smaller energy gap than $ZnFe_2O_4$, which is an n-type semiconductor. Consequently, a space charge region and a potential barrier formed at the interface between the two ferrites to achieve Fermi-level continuity, and the energy gap for $CuFe_2O_4$ on the $ZnFe_2O_4$ layer decreased to 1.78 eV. This decrease could be a result of the increase in the grain size of $CuFe_2O_4$, as it was grown on $ZnFe_2O_4$ [36].

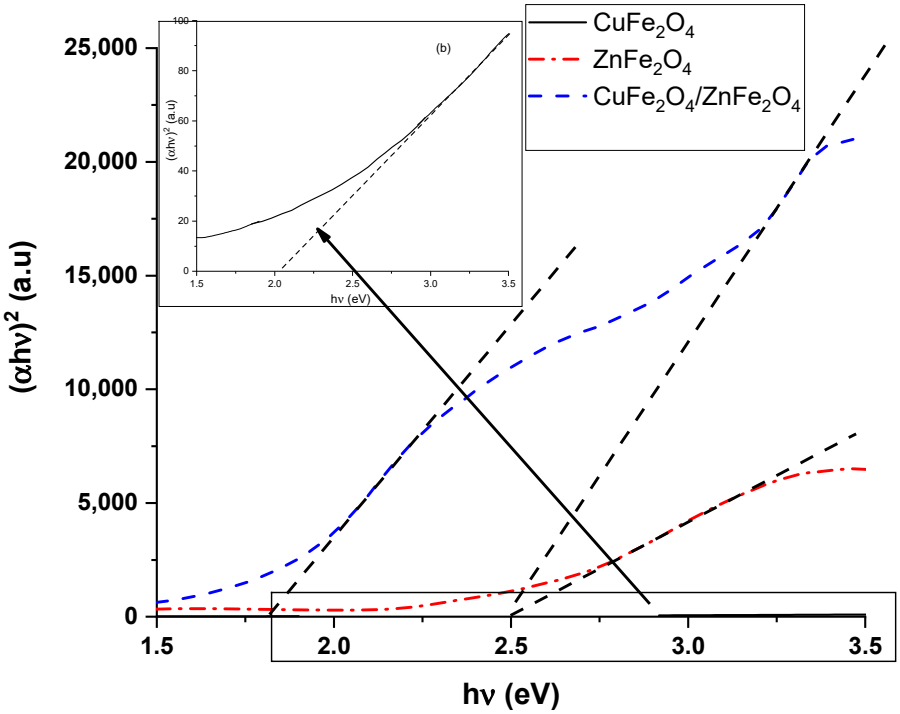

Figure 3. Tauc's plot analysis indicating the direct bandgap transition(s) for the investigated samples.

The presence of this barrier potential at the interface can reduce the recombination rate between electrons and holes, thereby influencing the photoluminescent intensity. Therefore, to determine the optical properties, photoluminescence (PL) measurements were conducted.

Figure 4 displays the PL emission spectra obtained at an excitation wavelength of 325 nm ($E_{exc.}$ = 3.8 eV), which exceeds the energy gaps of Zn ferrite and Cu ferrite. It is evident that the PL signal is stronger for Cu ferrite than for Zn ferrite, indicating a faster recombination rate of electron–hole pairs in Cu ferrite. Conversely, a slight decrease in the PL signal was observed for the p–n junction sample. This result can be attributed to the presence of a strong barrier potential at the $CuFe_2O_4/ZnFe_2O_4$ interface, as mentioned earlier.

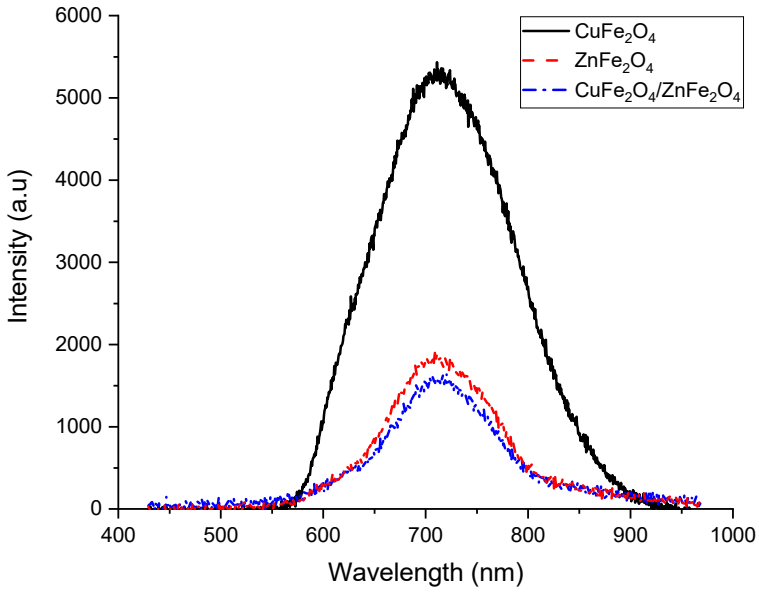

Figure 4. Photoluminescence spectra of the prepared samples.

3.3. Electrochemical Impedance Spectroscopy

The basic photoelectrochemical cell (PEC) parameters of fabricated photoelectrodes, including $CuFe_2O_4$, $ZnFe_2O_4$, and $CuFe_2O_4/ZnFe_2O_4$, were investigated under dark conditions using electrochemical impedance spectroscopy (EIS). EIS measurements were conducted with a voltage amplitude of 50 mV over the frequency range of 1.0 Hz–100 kHz. The resulting Nyquist plots (Figure 5) display distinct semicircles, indicating the charge transfer process at the electrode–electrolyte interface, while the semicircle diameter represents the charge transfer resistance.

Notably, the $CuFe_2O_4$ sample exhibited the largest diameter, indicative of slow charge transfer at the electrode–electrolyte interface, whereas the $ZnFe_2O_4$ sample displayed a smaller radius, signifying rapid and effective charge transfer [36,37]. Remarkably, the $CuFe_2O_4/ZnFe_2O_4$ electrode showed the smallest diameter of the semicircle, indicating a higher charge transfer rate, i.e., smaller charge transfer resistance and, consequently, a smaller recombination rate, suggesting a faster charge transfer and more efficient electron–hole pair separation. This finding suggests that the formation of a barrier potential at the $CuFe_2O_4/ZnFe_2O_4$ interface enhances electron–hole charge transfer.

Consequently, the $CuFe_2O_4/ZnFe_2O_4CuFe_2O_4/ZnFe_2O_4$ heterostructure holds promise as a potential photoanode for high-efficiency solar hydrogen generation due to its fast charge separation and transport capabilities.

The Mott–Schottky analysis was conducted to explore the band structure alignment of $CuFe_2O_4$ and $ZnFe_2O_4$ samples. Their valence and conduction band positions were assessed using the flat-band potential (V_{fb}) and bandgap values (E_g). Figure 6 depicts the Mott–Schottky (M-S) curves for $CuFe_2O_4$ and $ZnFe_2O_4$ samples, revealing a negative slope for $CuFe_2O_4$ (indicating a p-type semiconductor) and a positive slope for $ZnFe_2O_4$ (indicating an n-type semiconductor) [38,39]. The flat-band potential (V_{fb}) was determined by extrapolating the plot of $1/C^2$ versus the potential to the x-axis. For $ZnFe_2O_4$ and $CuFe_2O_4$, the flat-band potentials were −0.74 eV and 0.62 eV vs. Ag/AgCl, respectively. As the difference between the flat-band potential and the bottom/top edge of the conduction/valence band is negligible for n-type/p-type materials, we regard the flat-band potential as the conduction/valence band edge for n-type and p-type semiconductors, respectively [39]. From the flat-band positions and the band energy gaps, the band structure alignment between $ZnFe_2O_4$ and $CuFe_2O_4$ could be estimated.

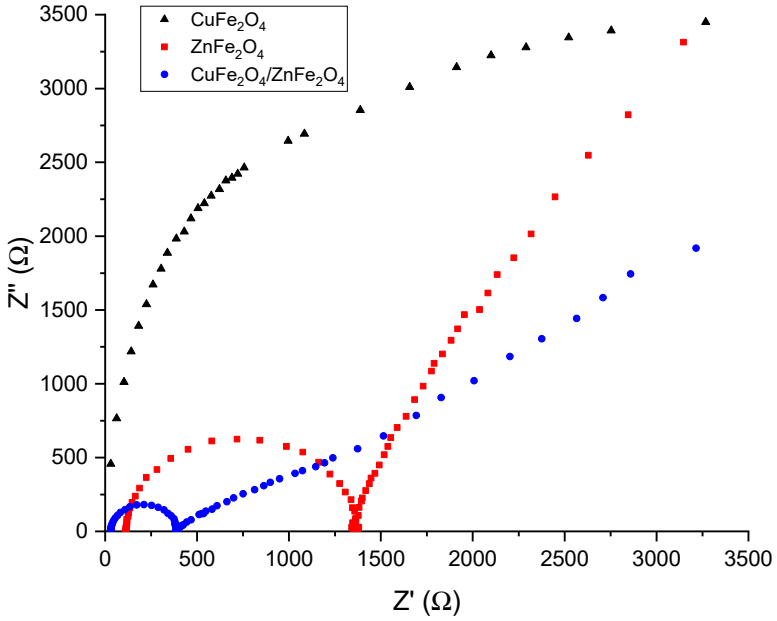

Figure 5. Nyquist plot of all investigated samples.

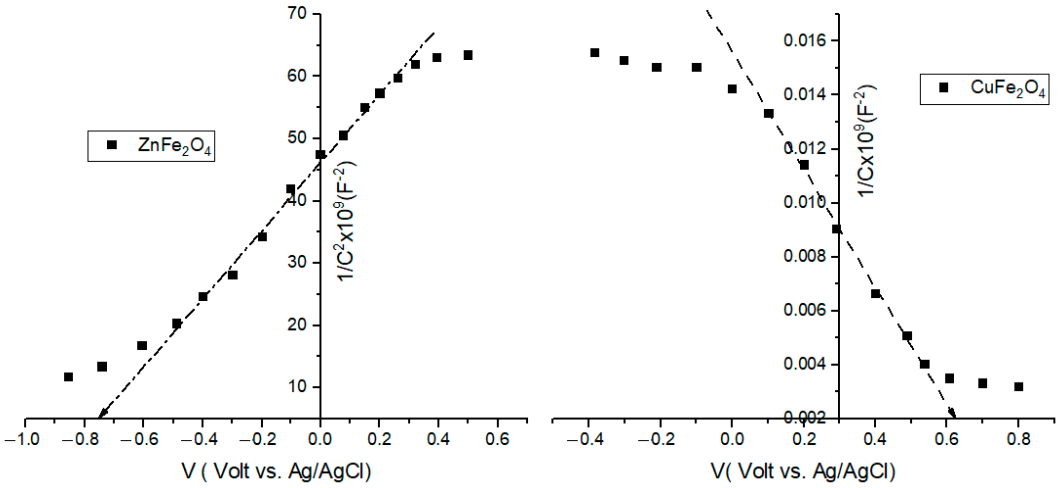

Figure 6. Mott–Schottky plots of $CuFe_2O_4$ and $ZnFe_2O_4$ samples.

Figure 7 depicts the proposed electronic band structure of the p–n junction between $CuFe_2O_4$ and $ZnFe_2O_4$ under the light condition of our experiment. Strong band bending occurs, leading to the generation of a high barrier potential at the interface. Due to the small thickness of the $CuFe_2O_4$ layer on $ZnFe_2O_4$, some photons are absorbed within the bulk of $ZnFe_2O_4$ (E_{g1}), while others are absorbed at the surface of $CuFe_2O_4$ (E_{g2}).

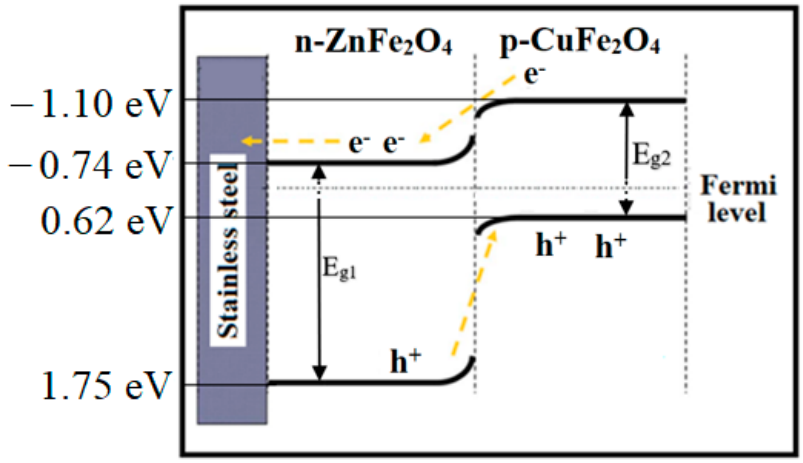

Figure 7. Energy band diagram of $CuFe_2O_4/ZnFe_2O_4$ p–n junction.

3.4. Linear Sweep Voltammetry (LSV) Measurements

A three-electrode configuration was employed using a photoelectrochemical cell (PEC) to investigate the photocurrent density–voltage (J-V) characteristics. The experimental setup is depicted in Figure 8. The modified stainless steel plate served as the working electrode (WE), graphite was used as the counter electrode (CE), and Ag/AgCl served as the reference electrode (RE). J-V measurements were conducted in an alkaline medium (0.3 M NaOH) using a 100-watt white LED source and a concentrated lens under both dark and illuminated conditions. All of the electric components of the experiment (power supply and LED light source) were supplied by a 500-watt solar panel system. The scanning speed rate was fixed at 10 mV/s.

Figure 9 presents the J-V curves for all samples. It is evident that both $CuFe_2O_4$ and $ZnFe_2O_4$ electrodes exhibited an onset potential of approximately 0.9 volts. Additionally, $CuFe_2O_4$ achieved its maximum current at 0.95 volts, while $ZnFe_2O_4$ reached its maximum current at 1.01 volts. The decrease in current beyond a certain anode potential is attributed to the onset of electrode oxidation at specific potentials (cathodic potential). Considering

that $CuFe_2O_4$ possesses two oxidation–reduction mechanisms ($Fe^{2+} \leftrightarrow Fe^{3+}$ and $Cu^{+1} \leftrightarrow Cu^{2+}$), and $ZnFe_2O_4$ has only one ($Fe^{2+} \leftrightarrow Fe^{3+}$), it can be concluded that the corrosion resistance of $ZnFe_2O_4$ is superior to that of $CuFe_2O_4$.

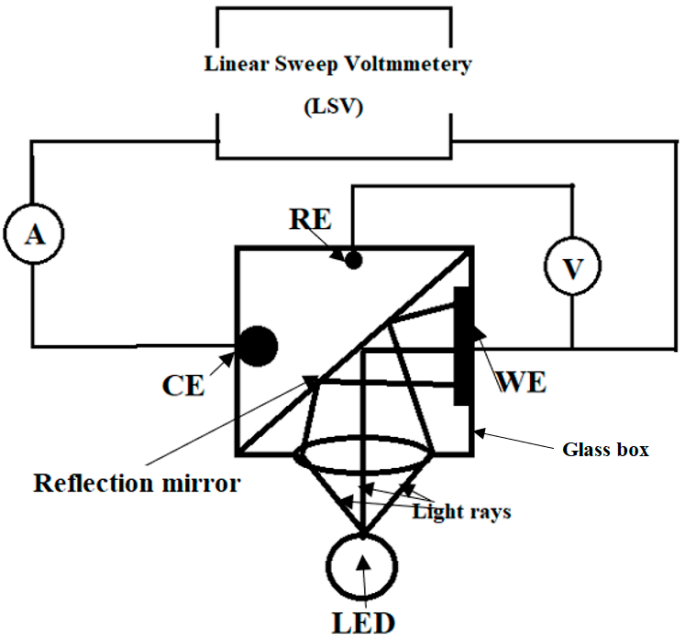

Figure 8. Experimental setup for measuring the J-V curve.

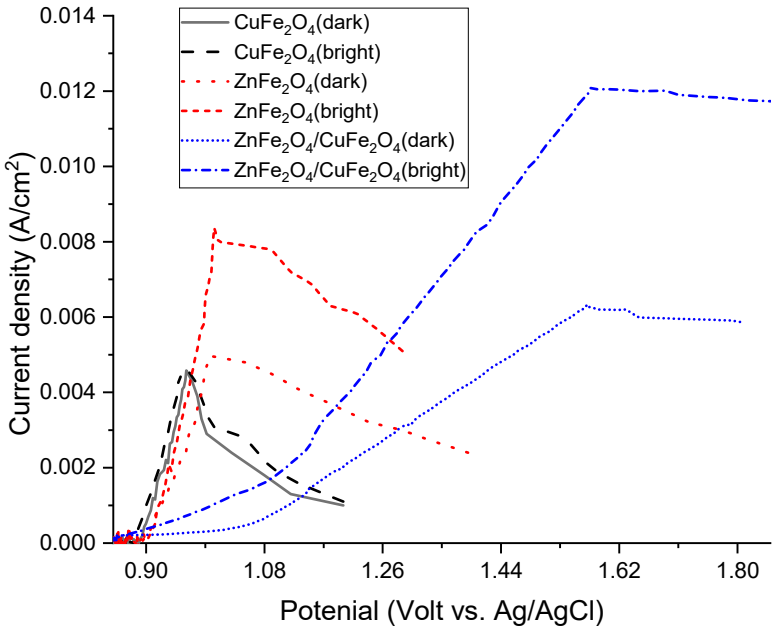

Figure 9. Linear sweep voltammetry (LSV) measurements for all prepared samples.

Moreover, the effect of illumination on the current density was more pronounced for $ZnFe_2O_4$ compared to $CuFe_2O_4$. This can be explained in terms of the recombination rate between the generated electron–hole pairs under light illumination. As discussed in the section regarding photoluminescence (PL) and electrochemical impedance spectroscopy (EIS) measurements, the PL signal and radius of the semicircles in Nyquist plots for $CuFe_2O_4$ were significantly greater than those for $ZnFe_2O_4$, indicating a higher recombination rate in $CuFe_2O_4$, which in turn affected the photogenerated current. The increase in photocurrent

for both Cu ferrite and Zn ferrite was attributed to the enhanced photoconductivity of the samples.

For the p–n junction sample, it is noteworthy that the starting potential was 1.05 volts, and the anodic voltage was 1.57 volts, indicating improved corrosion resistance. Indeed, the performance remains lower than the other samples until reaching 1.44 V (vs. Ag/AgCl) due to the altered bandgap of the $CuFe_2O_4$ layer. This alteration causes the band binding for the holes to be greater than that of the electrons (see Figure 7). In other words, the separation rate of generated holes on the Zn ferrite side is faster than the separation rate of generated electrons on the Cu ferrite side, increasing the likelihood of recombination between the holes and electrons. At an applied voltage of 1.44 V (vs. Ag/AgCl), it appears that the rate of electron separation becomes sufficiently fast to overcome recombination with holes. Furthermore, the $CuFe_2O_4$ material itself might hinder changes despite the improved charge separation. Additionally, the effect of illumination on the generated current was more pronounced for the p–n junction sample compared to the other electrodes. These results can be explained by considering the suggested p–n junction electronic band diagram, which demonstrates the generation of an internal electric potential. This facilitates the transfer of photogenerated holes to $CuFe_2O_4$, while more photogenerated electrons can be transferred to the conductive substrate via the $ZnFe_2O_4$ layer. Furthermore, the presence of electron trapping at the interface reduced the recombination rate between the photogenerated electrons and holes, leading to an enhancement in photoelectrochemical performance.

Based on these findings, it is evident that the p–n junction sample, which acts as a photoanode, offers significant advantages for hydrogen generation, particularly under illuminated conditions.

3.5. Evaluation of Hydrogen Production Rate

In this part of the study, the hydrogen production rate (HPR) for the samples was evaluated under both dark and illuminated conditions at a fixed voltage of 1.5 volts (vs. AgCl/Ag) over a period of 10 h. Figure 10 illustrates the relationship between HPR and time. It is apparent that the steady state of production is reached after approximately 1 h of the experiment, and the production rate remains relatively constant throughout the duration of the experiment. This indicates a high corrosion resistance of the modified electrodes. Furthermore, a significant increase in HPR was observed under light illumination.

The HPR under illumination exhibited an enhancement of approximately 30% compared to the measurements taken in the dark. The mechanism of hydrogen production under illumination is depicted in Figure 11.

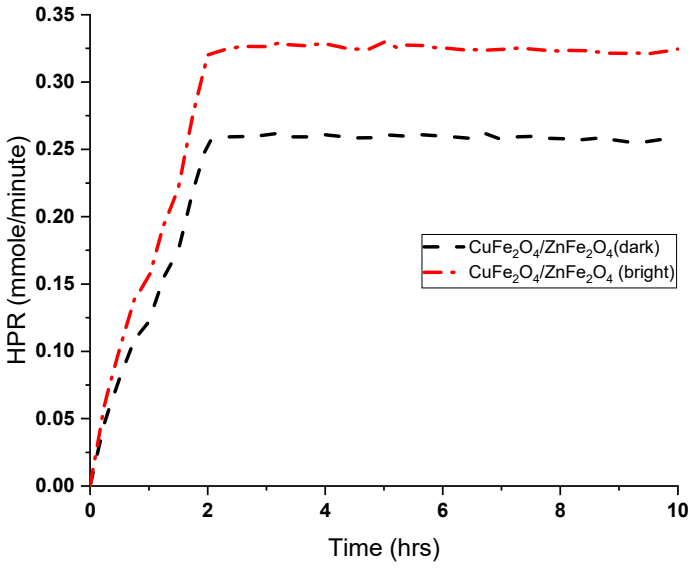

Figure 10. Hydrogen production rate (HPR) at V = 1.5 volts versus time.

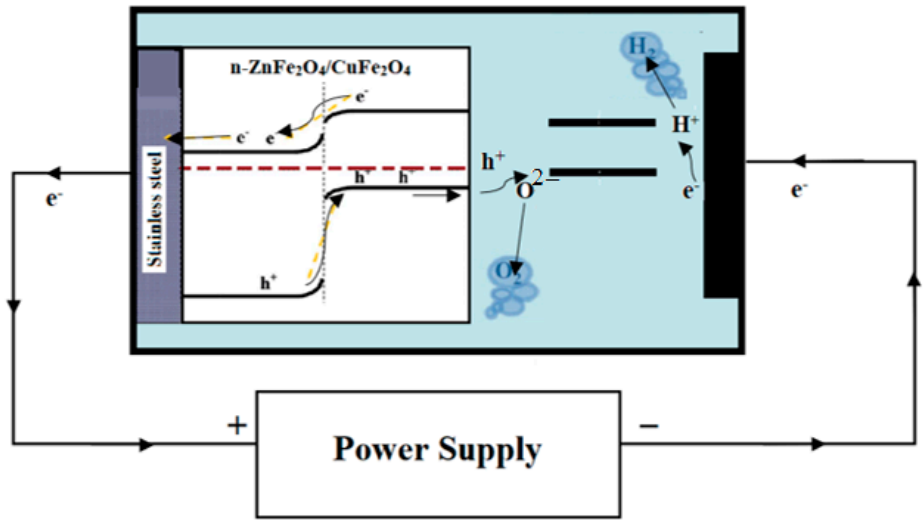

Figure 11. Mechanism of hydrogen evolution using $CuFe_2O_4/ZnFe_2O_4$ p–n junction.

To examine the effect of photoelectrolysis over 10 h on the crystal and surface structures of the $CuFe_2O_4/ZnFe_2O_4$ p–n junction, XRD and SEM patterns were compared before and after the hydrogen production experiment. Figures 12 and 13 show the XRD chart and the SEM images before and after the experiment, respectively. The XRD chart indicates that the structure remains a single crystal ferrite even after 10 h of experimentation, demonstrating the chemical stability of the sample during prolonged hydrogen production. Furthermore, the SEM images revealed minimal changes in surface morphology; the sample became smoother, except for some etching, particularly at the grain boundaries. This study highlights the good chemical and physical stability of the investigated sample during hydrogen production.

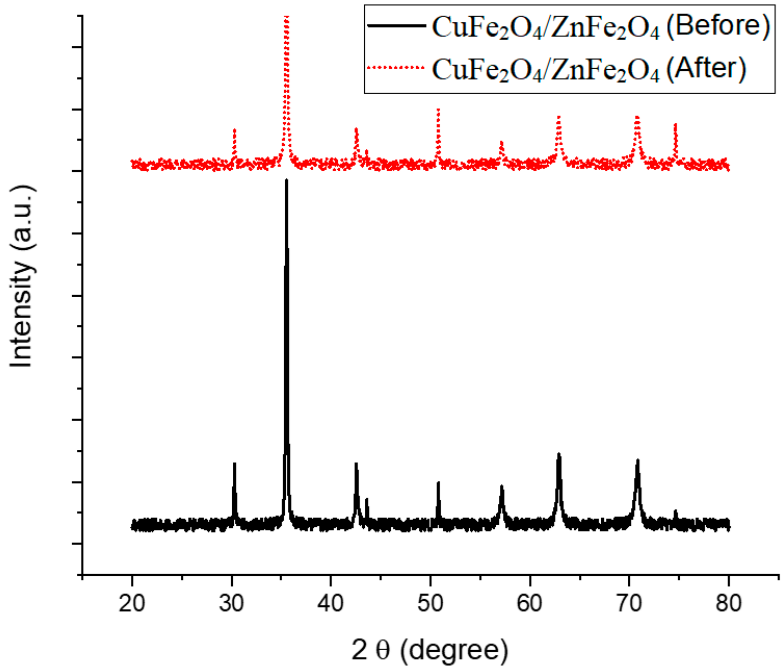

Figure 12. XRD charts for $CuFe_2O_4/ZnFe_2O_4$ junction before and after hydrogen production.

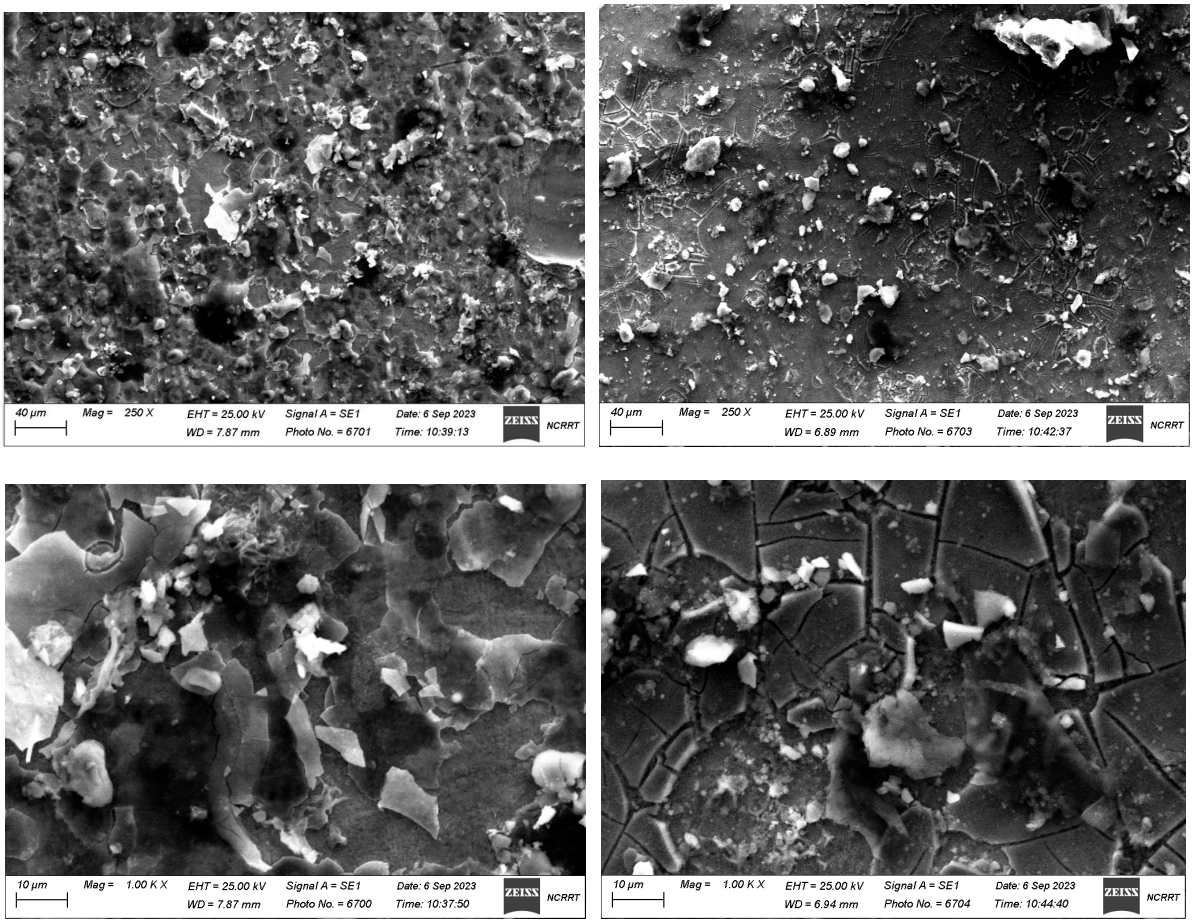

Figure 13. SEM images of the sample before and after hydrogen production at magnifications of x = 250 and Kx = 1.

SEM images show a highly rough surface structure, which results from the spray pyrolysis method of preparation, affecting the quality of the prepared samples. For future studies, a new method of thin film preparation, such as atomic layer deposition (ALD), may be used to enhance PEC cell performance.

4. Conclusions

The implementation of a $CuFe_2O_4/ZnFe_2O_4$ heterojunction demonstrated a significant improvement in the hydrogen production rate, achieving an enhancement of approximately 30%. This enhancement can be attributed to the presence of an interfacial barrier potential, which effectively reduces electron–hole recombination rates. Consequently, the photocatalytic effects were more pronounced, leading to improved performance at the electrolyte–electrode interface. Additionally, coating stainless steel with this ferrite compound resulted in enhanced corrosion resistance. The investigated sample exhibits good chemical and physical stability after a relatively long period of hydrogen production.

Funding: This research received no external funding.

Data Availability Statement: Data is contained within the article.

Conflicts of Interest: The authors declare no conflict of interest.

References

1. Tolod, K.R.; Hernández, S.; Russo, N. Recent Advances in the $bivo_4$ Photocatalyst for Sun-Driven Water Oxidation: Top-Performing Photoanodes and Scale-Up Challenges. *Catalysts* **2016**, *7*, 13. [CrossRef]

2. Ho-Kimura, S.; Moniz, S.J.A.; Handoko, A.D.; Tang, J. Enhanced photoelectrochemical water splitting by nanostructured $BiVO_4$–TiO_2 composite electrodes. *J. Mater. Chem. A* **2014**, *2*, 3948–3953. [CrossRef]
3. Gholipour, M.R.; Dinh, C.-T.; Béland, F.; Do, T.-O. Nanocomposite heterojunctions as sunlight-driven photocatalysts for hydrogen production from water splitting. *Nanoscale* **2015**, *7*, 8187–8208. [CrossRef] [PubMed]
4. Chiarello, G.L.; Selli, E. Photocatalytic hydrogen production. *Recent Patents Eng.* **2010**, *4*, 155–169. [CrossRef]
5. Liao, C.-H.; Huang, C.-W.; Wu, J.C.S. Hydrogen Production from Semiconductor-based Photocatalysis via Water Splitting. *Catalysts* **2012**, *2*, 490–516. [CrossRef]
6. Moniz, S.J.A.; Shevlin, S.A.; Martin, D.J.; Guo, Z.-X.; Tang, J. Visible-light driven heterojunction photocatalysts for water splitting—A critical review. *Energy Environ. Sci.* **2015**, *8*, 731–759. [CrossRef]
7. Zhou, L.; Wang, W.; Liu, S.; Zhang, L.; Xu, H.; Zhu, W. A sono-chemical route to visible-light-driven high-activity $BiVO_4$ photocatalyst. *J. Environ. Sci.* **2006**, *24*, 449–457. [CrossRef]
8. Zhang, L.; Li, Y.; Zhang, Q.; Wang, H. Hierarchical nanostructure of WO3 nanorods on TiO_2 nanofibers and the enhanced visible light photocatalytic activity for degradation of organic pollutants. *CrystEngComm* **2013**, *15*, 5986–5993. [CrossRef]
9. Mallesh, S.; Srinivas, V. A comprehensive study on thermal stability and magnetic properties of MnZn-ferrite nanoparticles. *J. Magn. Magn. Mater.* **2018**, *475*, 290–303. [CrossRef]
10. Bastianello, M.; Gross, S.; Elm, M.T. Thermal stability, electrochemical and structural characterization of hydrothermally synthesised cobalt ferrite ($CoFe_2O_4$). *RSC Adv.* **2019**, *9*, 33282–33289. [CrossRef]
11. Hammad, T.M.; Salem, J.K.; Abu Amsha, A.; Hejazy, N.K. Optical and magnetic characterizations of zinc substituted copper ferrite synthesized by a co-precipitation chemical method. *J. Alloy. Compd.* **2018**, *741*, 123–130. [CrossRef]
12. Joshi, G.P.; Saxena, N.S.; Mangal, R.; Mishra, A.; Sharma, T.P. Band gap determination of Ni-Zn ferrites. *Bull. Mater. Sci.* **2003**, *26*, 387–389. [CrossRef]
13. Azab, A.A.; Mansour, A.M.; Turky, G.M. Structural, Magnetic, and Dielectric properties of $Sr_4Fe_6O_{13}$ ferrite prepared of small crystallites. *Sci. Rep.* **2020**, *10*, 4955. [CrossRef]
14. Ismael, M. Ferrites as solar photocatalytic materials and their activities in solar energy conversion and environmental protection: A review. *Sol. Energy Mater. Sol. Cells* **2020**, *219*, 110786. [CrossRef]
15. Reddy, D.H.K.; Yun, Y.-S. Spinel ferrite magnetic adsorbents: Alternative future materials for water purification? *Coord. Chem. Rev.* **2016**, *315*, 90–111. [CrossRef]
16. ElNahrawy, A.M.; Mansour, A.M.; ElAttar, H.A.; Sakr, E.M.M.; Soliman, A.A.; Hammad, A.B.A. Impact of Mn-substitution on structural, optical, and magnetic properties evolution of sodium–cobalt ferrite for opto-magnetic applications. *J. Mater. Sci. Mater. Electron.* **2020**, *31*, 6224–6232. [CrossRef]
17. Jang, Y.J.; Bin Park, Y.; Kim, H.E.; Choi, Y.H.; Choi, S.H.; Lee, J.S. Oxygen-Intercalated $CuFeO_2$ Photocathode Fabricated by Hybrid Microwave Annealing for Efficient Solar Hydrogen Production. *Chem. Mater.* **2016**, *28*, 6054–6061. [CrossRef]
18. Jiang, J.; Fan, W.; Zhang, X.; Bai, H.; Liu, Y.; Huang, S.; Mao, B.; Yuan, S.; Liu, C.; Shi, W. Rod-in-tube nanostructure of $MgFe_2O_4$: Electrospinning synthesis and photocatalytic activities of tetracycline. *New J. Chem.* **2016**, *40*, 538–544. [CrossRef]
19. Guijarro, N.; Bornoz, P.; Prévot, M.; Yu, X.; Zhu, X.; Johnson, M.; Jeanbourquin, X.; Le Formal, F.; Sivula, K. Evaluating spinel ferrites MFe_2O_4 (M = Cu, Mg, Zn) as photoanodes for solar water oxidation: Prospects and limitations. *Sustain. Energy Fuels* **2018**, *2*, 103–117. [CrossRef]
20. Kim, J.H.; Jang, Y.J.; Kim, J.H.; Jang, J.-W.; Choi, S.H.; Lee, J.S. Defective $ZnFe_2O_4$ nanorods with oxygen vacancy for photoelectrochemical water splitting. *Nanoscale* **2015**, *7*, 19144–19151. [CrossRef]
21. Karim, K.M.R.; Ong, H.R.; Abdullah, H.; Yousuf, A.; Cheng, C.K.; Khan, M.R. Photoelectrochemical reduction of carbon dioxide to methanol on p-type CuFe2O4 under visible light irradiation. *Int. J. Hydrogen Energy* **2018**, *43*, 18185–18193. [CrossRef]
22. Tarek, M.; Karim, K.M.R.; Sarkar, S.M.; Deb, A.; Ong, H.R.; Abdullah, H.; Cheng, C.K.; Khan, M.R. Hetero-structure CdS–$CuFe_2O_4$ as an efficient visible light active photocatalyst for photoelectrochemical reduction of CO_2 to methanol. *Int. J. Hydrogen Energy* **2019**, *44*, 26271–26284. [CrossRef]
23. Duan, K.; Que, T.; Koppala, S.; Balan, R.; Lokesh, B.; Pillai, R.; David, S.; Karthikeyan, P.; Ramamoorthy, S.; Lekshmi, I.C.; et al. A facile route to synthesize n-SnO_2/p-$CuFe_2O_4$ to rapidly degrade toxic methylene blue dye under natural sunlight. *RSC Adv.* **2022**, *12*, 16544–16553. [CrossRef] [PubMed]
24. Balatskiy, D.; Budnikova, Y.; Bratskaya, S.; Vasilyeva, M. TiO_2-$CoFe_2O_4$ and TiO_2-$CuFe_2O_4$ Composite Films: A New Approach to Synthesis, Characterization, and Optical and Photocatalytic Properties. *J. Compos. Sci.* **2023**, *7*, 295. [CrossRef]
25. Liu, Z.; Zhao, Z.-G.; Miyauchi, M. Efficient Visible Light Active $CaFe_2O_4$/WO_3 Based Composite Photocatalysts: Effect of Interfacial Modification. *J. Phys. Chem. C* **2009**, *113*, 17132–17137. [CrossRef]
26. Kim, E.S.; Kang, H.J.; Magesh, G.; Kim, J.Y.; Jang, J.-W.; Lee, J.S. Improved Photoelectrochemical Activity of $CaFe_2O_4$/$BiVO_4$ Heterojunction Photoanode by Reduced Surface Recombination in Solar Water Oxidation. *ACS Appl. Mater. Interfaces* **2014**, *6*, 17762–17769. [CrossRef] [PubMed]
27. Elzwawy, A.; Mansour, A.; Magar, H.S.; Hammad, A.B.A.; Hassan, R.Y.; El Nahrawy, A.M. Exploring the structural and electrochemical sensing of wide bandgap calcium phosphate/$CuxFe_3$-xO_4 core-shell nanoceramics for H_2O_2 detection. *Mater. Today Commun.* **2022**, *33*, 104574. [CrossRef]

28. Ahmed, M.G.; Kandiel, T.A.; Ahmed, A.Y.; Kretschmer, I.; Rashwan, F.; Bahnemann, D. Enhanced Photoelectrochemical Water Oxidation on Nanostructured Hematite Photoanodes via p-$CaFe_2O_4$/n-Fe_2O_3 Heterojunction Formation. *J. Phys. Chem. C* **2015**, *119*, 5864–5871. [CrossRef]
29. Lee, S.Y.; Huang, E.-W.; Woo, W.; Yoon, C.; Chae, H.; Yoon, S.-G. Dynamic Strain Evolution around a Crack Tip under Steady- and Overloaded-Fatigue Conditions. *Metals* **2015**, *5*, 2109–2118. [CrossRef]
30. Najmoddin, N.; Beitollahi, A.; Kavas, H.; Mohseni, S.M.; Rezaie, H.; Åkerman, J.; Toprak, M.S. XRD cation distribution and magnetic properties of mesoporous Zn-substituted $CuFe_2O_4$. *Ceram. Int.* **2014**, *40*, 3619–3625. [CrossRef]
31. Tatarchuk, T.; Bououdina, M.; Macyk, W.; Shyichuk, O.; Paliychuk, N.; Yaremiy, I.; Al-Najar, B.; Pacia, M. Structural, Optical, and Magnetic Properties of Zn-Doped $CoFe_2O_4$ Nanoparticles. *Nanoscale Res. Lett.* **2017**, *12*, 141. [CrossRef] [PubMed]
32. Somnath; Batoo, K.M.; Raslan, E.H.; Adil, S.F.; Sharma, I.; Kumar, G. Correction to: Investigation of electrical, magnetic, and optical properties of silver-substituted magnesium–manganese ferrite nanoparticles. *J. Mater. Sci. Mater. Electron.* **2020**, *31*, 10939. [CrossRef]
33. Karnaji; Nurhasanah, I. Photodegradation of Rhodamine B by using $ZnFe_2O_4$ Nanoparticles Synthesized through Precipitation Method. *IOP Conf. Ser. Mater. Sci. Eng.* **2017**, *202*, 012044. [CrossRef]
34. Park, S.; Baek, J.H.; Zhang, L.; Lee, J.M.; Stone, K.H.; Cho, I.S.; Guo, J.; Jung, H.S.; Zheng, X. Rapid Flame-Annealed $CuFe_2O_4$ as Efficient Photocathode for Photoelectrochemical Hydrogen Production. *ACS Sustain. Chem. Eng.* **2019**, *7*, 5867–5874. [CrossRef]
35. Kumar, K.V. Tunable Optical Bandgap of Gadolinium Substituted Nickel-Zinc Ferrite Nanoparticles-Effect of Calcination Temperature on Its Optical Parameters. *Adv. Mater. Phys. Chem.* **2022**, *12*, 33–45. [CrossRef]
36. Shetty, K.; Renuka, L.; Nagaswarupa, H.P.; Nagabhushana, H.; Anantharaju, K.S.; Rangappa, D.; Prashantha, S.C.; Ashwini, K. A comparative study on $CuFe_2O_4$, $ZnFe_2O_4$ and $NiFe_2O_4$: Morphology, Impedance and Photocatalytic studies. *Mater. Today Proc.* **2017**, *4*, 11806–11815. [CrossRef]
37. Belhadj, H.; Messaoudi, Y.; Khelladi, M.R.; Azizi, A. A facile synthesis of metal ferrites (MFe_2O_4, M = Co, Ni, Zn, Cu) as effective electrocatalysts toward electrochemical hydrogen evolution reaction. *Int. J. Hydrogen Energy* **2022**, *47*, 20129–20137. [CrossRef]
38. Preethi, S.; Vivek, S.; Priya, R.; Balakumar, S.; Babu, K.S. Enhanced photocatalytic performance of $CuFeO_2$-ZnO heterostructures for methylene blue degradation under sunlight. *J. Mater. Sci. Mater. Electron.* **2021**, *32*, 22256–22269. [CrossRef]
39. Zhang, M.; Xie, X.; Si, Y.; Gao, J.; Du, H.; Pei, S.; Zhang, X.; Yan, Q. Enhanced photocatalytic performance of $ZnFe_2O_4$/BiOI hybrid for the degradation of methyl orange. *J. Mater. Sci. Mater. Electron.* **2019**, *30*, 8055–8063. [CrossRef]